

# Phase-Contrast Imaging and Tomography at 60 keV using a Conventional X-ray Tube

T. Donath\*<sup>a</sup>, F. Pfeiffer<sup>a,b</sup>, O. Bunk<sup>a</sup>, W. Groot<sup>a</sup>, M. Bednarzik<sup>a</sup>, C. Grünzweig<sup>a</sup>, E. Hempel<sup>c</sup>,  
S. Popescu<sup>c</sup>, M. Hoheisel<sup>c</sup>, C. David<sup>a</sup>

<sup>a</sup>Paul Scherrer Institut, 5232 Villigen PSI, Switzerland;

<sup>b</sup>Ecole Polytechnique Fédérale de Lausanne, 1015 Lausanne, Switzerland;

<sup>c</sup>Siemens AG, Healthcare Sector, 91301 Forchheim, Germany

## ABSTRACT

Phase-contrast imaging using grating interferometers has been developed over the last few years for x-ray energies of up to 28 keV. We have now developed a grating interferometer for phase-contrast imaging that operates at 60 keV x-ray energy. Here, we show first phase-contrast projection and CT images recorded with this interferometer using an x-ray tube source operated at 100 kV acceleration voltage. By comparison of the CT data with theoretical values, we find that our measured phase images represent the refractive index decrement at 60 keV in good agreement with the theoretically expected values. The extension of phase-contrast imaging to this significantly higher x-ray energy opens up many new applications of the technique in industry, medicine, and research.

**Keywords:** hard x-ray, phase contrast; computed tomography; CT; grating interferometry; Talbot effect; complex refractive index

## 1. INTRODUCTION

The contrast in conventional x-ray radiography and CT arises from the attenuation of x-rays (by absorption or scatter processes) in the examined object. Differential phase-contrast (DPC) radiography and tomography has been developed over the last few years [1-6] and allows for the simultaneous measurement of the conventional attenuation signal and an additional phase signal, within a single measurement. The method was first demonstrated at synchrotron-radiation x-ray sources using an intense and almost parallel x-ray beam with a narrow wavelength spectrum, i.e. an x-ray beam with high brilliance [1-2,5]. In parallel to these measurements, this phase-contrast method was extended to work with conventional low-brilliance x-ray tube sources [3-4,6].

So far, the x-ray grating interferometer has been used up to x-ray energies of 28 keV. For phase-contrast imaging, this x-ray regime has been referred to as "hard x-ray" energy range. This somewhat arbitrary notation arises from the difficulty to perform phase-contrast measurements at or above this x-ray energy. The major difficulty for the grating interferometer in going to higher x-ray energies arises in the micro-fabrication of periodic one-dimensional gratings with structure heights that are sufficiently high and result in enough phase shift and absorption of the penetrating x rays.

### 1.1 Differential phase-contrast projections

The scheme in Figure 1 shows the principle of projection imaging with a grating interferometer. Here, in contrast to conventional radiography, not only the intensity of x-rays but also their deflection angle is determined. Figure 1a schematically shows the deflection of x-rays penetrating a cylindrical object.

\*tilman.donath@psi.ch; phone +41 56 310-4630; www.psi.ch

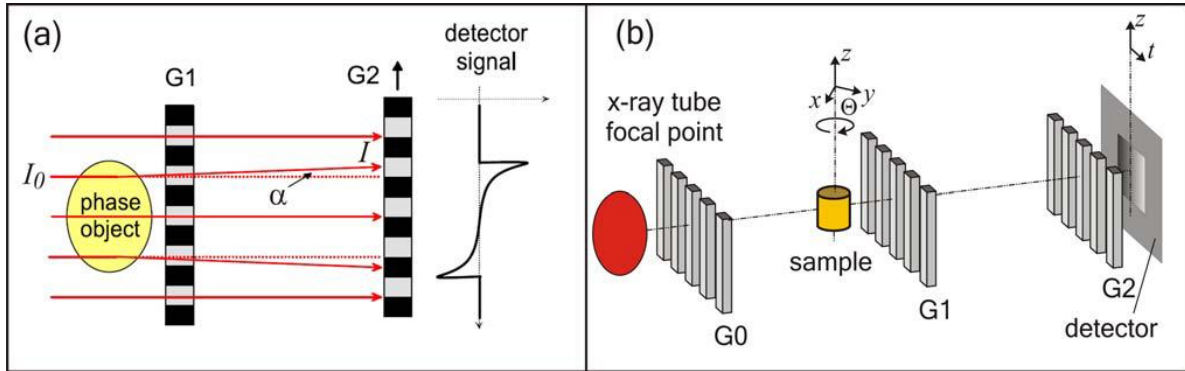


Fig. 1. Phase-contrast measurement using a grating interferometer. (a) The beam deflection caused by the sample is transformed into an intensity variation that is detected with a conventional two-dimensional x-ray detector. During a phase-stepping scan, grating G2 is moved stepwise perpendicular to the grating structures, while the intensity oscillation is recorded for each detector pixel. (b) Arrangement of the symmetric grating interferometer using a conventional x-ray tube source. The interferometer consists of two absorption gratings G0 and G2 and one phase grating G1.

For the conventional radiography image, the attenuation (or transmission) signal is determined from the ratio of the intensity  $I_0$  of the x-ray beam without the sample in the beam and the intensity  $I$  of the x-ray beam that has penetrated the sample. From these measurements, the projection

$$p = -\ln \frac{I}{I_0} = \int ds \mu(x, y, z) \quad (1)$$

is calculated. The right hand side of this equation describes the projection of the linear attenuation coefficient  $\mu(x, y, z)$  along the x-ray path  $s$ .

The additional phase signal is simply the deflection angle, i.e. the angle between the reference beam without the sample and the transmitted x-ray beam, when the sample is inserted. The deflection is approximately given by

$$\alpha = \frac{\partial}{\partial t} \int ds \delta(x, y, z), \quad (2)$$

where

$$n = 1 - \delta + i\beta \quad (3)$$

is the complex refractive index of the sample. Here, the imaginary part  $\beta$  of the refractive index describes the attenuation of x-rays and is related to the linear attenuation coefficient as  $\beta = \mu\lambda(4\pi)^{-1}$  for x-ray wavelength  $\lambda$ , while the real part  $\delta$ , which is called the refractive index decrement, determines the phase shift and the deflection angle caused by the sample. The direction of the partial derivative in Equation 2 is perpendicular to the grating structures and explains the differential nature of the differential phase-contrast images. Integration in Equation 2 is performed along the x-ray path  $s$ .

## 1.2 Projections from phase scans

The grating interferometer allows us to measure intensity and propagation direction of the x-ray beam simultaneously and independently for each detector pixel. Due to the Talbot effect, the grating structure of G1 is reproduced as an interference pattern in the plane of G2. G2 has the same periodicity as the interference pattern. The relative position of the interference pattern and the G2 grating determines the amount of x-ray intensity that is transmitted through G2. This enables us to determine the relative position in a so-called phase-stepping scan, in which the intensity oscillation is recorded for each detector pixel, while the G2 grating is stepped an integer number of steps over a distance

corresponding to one or several times its period  $p_2$ . From the recorded phase-stepping scan, both the transmitted intensity and the deflection angle are calculated. The transmitted intensity is simply given by the average of all data points, while the relative position of interference pattern and G2 is deduced from the phase of the first Fourier component of a fast Fourier transform of the recorded oscillations for each pixel. The change of this phase determines the deflection angle caused by introduction of the sample. Thus, the conventional and the phase signal are simultaneously obtained from a single phase-stepping scan.

Recently, a method to measure a third, so-called dark-field image with the grating interferometer was proposed and demonstrated [7]. This scatter-related signal is given by the decrease of the oscillation amplitude in the phase-stepping scan of each pixel, when the sample is brought into the beam. The dark-field signal can also be recorded with the here presented interferometer setup for 60 keV. The results of these measurements shall be discussed in a separate publication.

### 1.3 Tomographic reconstruction

In conventional tomography, two-dimensional projection images  $p_d(t,z)$  recorded for many different projection angles  $\theta$  can be used to reconstruct the three-dimensional distribution of the attenuation coefficient  $\mu(x,y,z)$  inside the sample. This is done in conventional CT and is also possible with the conventional projection images obtained from the grating interferometer.

From the phase-contrast projections  $\alpha(t,z)$ , we can additionally reconstruct the distribution of the refractive index decrement  $\delta(x,y,z)$  inside the sample. In the reconstruction of the phase-contrast projections, however, we have to consider the differential nature of these projections. Applying a modified filtered-backprojection algorithm for the reconstruction, with an imaginary  $\text{sign}(f)$  frequency filter (Hilbert filter) instead of the usual ramp-function frequency filter  $|f|$ , correctly accounts for this behavior [6,8].

Together, the reconstructed signals  $\mu(x,y,z)$  and  $\delta(x,y,z)$  describe the entire complex refractive index distribution given in Equation 3.

## 2. GRATING-INTERFEROMETER SETUP FOR 60 KEV

Our grating interferometer is designed for the operation with x-ray tube sources and consists of three gratings, as shown in Figure 1b. G1 is a pi-shifting phase grating. The projection of G1 gives a periodic intensity distribution in the plane of G2 with the same frequency as G2. Grating G2 is an absorbing grating positioned in the 1st Talbot plane behind G1, and grating G0 is an absorbing grating that maintains the spatial coherence properties even for the extended source point of an x-ray tube. (For a spatially coherent source, e.g. an x-ray source with a very small source point, only gratings G1 and G2 are required.)

All gratings, i.e. the absorption gratings G0, G2, and the phase grating G1, were produced with the same period of  $p_0 = p_1 = p_2 = 8.5 \mu\text{m}$ . The equal periods result in a symmetric grating geometry, in which the G0-to-G1 and the G1-to-G2 distances are equal as can easily be deduced from the Talbot imaging formulas (compare Weitkamp et al. [1]). Hence, we refer to this geometry as a symmetric grating interferometer. The current design with equal period of all gratings reduced the grating production time, since G0 and G2 could be manufactured within the same process.

Table 1. Parameters of the constructed symmetric grating interferometer for 60 keV.

<b>Grating interferometer for 60 keV (0.2066 Å)</b>	
<u>Geometrical parameters</u>	
G0-G1 distance	875 mm
G1-G2 distance	875 mm
Talbot order	1st
<u>Grating parameters (material, period, structure height)</u>	
G0, G2 (absorbing)	Au, 8.5 μm, 90 μm
G1 (pi-shifting)	Si, 8.5 μm, 75 μm

The interferometer gratings were produced on 100 mm silicon wafers using photolithography, wet etching into silicon, and electro-plating of gold [9]. They were placed with their lines perpendicular to the optical axis of the interferometer and parallel to the axis of tomographic rotation as shown in Figure 1a. The G1 grating was produced in silicon with a structure height of  $h_1 = 75 \mu\text{m}$ , which is the Si-thickness that produces a phase shift of one-half wavelength at the photon energy of 60 keV. The G0 and G2 gratings were produced using a frequency-doubling technique [9], in which a Silicon structure of the double period was covered with a gold structure of height  $h_0 = h_2 = 90 \mu\text{m}$ . The parameters of our grating-interferometer are summarized in Table 1.

### 2.1 X-ray tube and x-ray camera

The grating interferometer is operated within a conventional radiography setup consisting of x-ray tube and x-ray camera. The x-ray tube in our setup is a MXR-160HP/11 of Comet AG, a water-cooled fixed anode tube with a tungsten target and a target angle of  $11^\circ$ . For the measurements presented here, the tube was operated at 100 kV, 10 mA, and with an effective source point of 1 mm diameter. The beam was pre-filtered by 30 mm of aluminum. The resulting x-ray spectrum has a mean energy of about 65 keV.

The x-ray camera in our setup is a self-built device based on lens-coupled imaging of a luminescent screen. It consists of a CsI scintillator of Hamamatsu (columnar growth CsI with a structure height of  $600 \mu\text{m}$ ) that converts the x-rays into visible light. The visible light image is projected over a  $90^\circ$  deflecting mirror and an objective lens onto a CCD camera (Proline of Finger Lakes Instrumentation) with  $1024 \times 1024$  pixels corresponding to a field of view of  $65 \times 65$  mm. To match the geometrical resolution of the realized setup and in order to speed up the measurements, the camera was operated in binning mode, with a binning factor of two in our measurements.

## 3. RESULTS

The grating interferometer for 60 keV was built and tested at the Laboratory for Micro- and Nanotechnology at the Paul Scherrer Institut. After the first alignment of the interferometer, we measured a fringe visibility of  $\sim 3\%$ , which is significantly lower than what was expected from simulations (8%) for the given design parameters. The deviation of the measured visibility was most likely due to imperfections in the first set of micro-structured gratings that we used. By now, we have replaced the gratings with a second set of gratings, and thereby increased the visibility to about 8%. However, the first set of gratings with its rather lower visibility was used to recorded projection images of several objects. Also a CT measurement of a simple test object was performed.

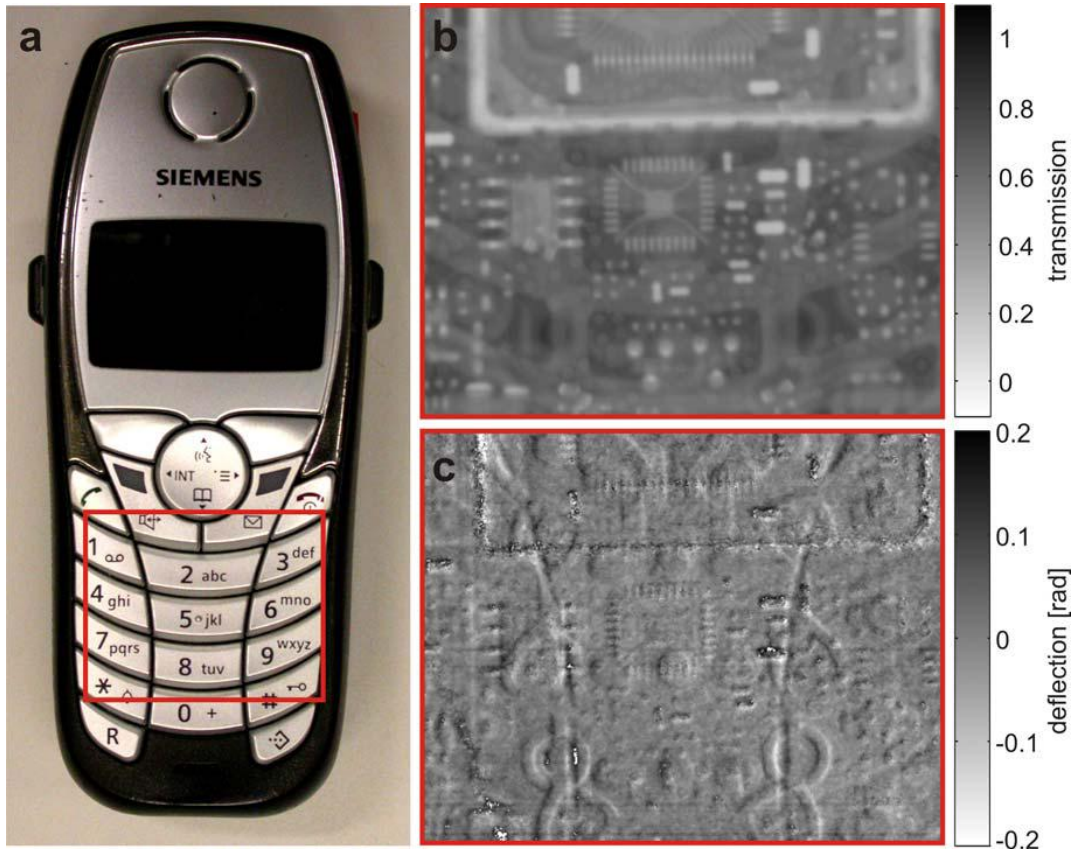


Fig. 2. Phase-contrast projections of a mobile phone. (a) Photograph with a rectangular box showing the location of (b) the conventional transmission image and (c) the phase-contrast image. The phase-contrast image shows the deflection angle in units of the phase shift of the oscillation in the phase-stepping scan. Both images were derived from the same phase-stepping data, with 16 phase steps recorded over one period of G2. The data were recorded at an x-ray tube setting of 100 kV, 10 mA with 3 seconds exposure per phase step.

### 3.1 Projection images

Projection images of a mobile phone are shown in Figure 2. The projection images show a region of  $451 \times 357$  pixels (at binning factor 2), which correspond to an area of  $28.7 \times 22.7$  mm at the sample position. One can immediately see the different nature of the conventional (Fig. 2b) and the phase-contrast image (Fig. 2c). The phase-contrast image is a directional image showing the directional derivative (from left to right) of the phase projection as described by Equation 2. Thus, vertical edges appear more pronounced in the phase image. Besides this difference, we find that different structures become visible in both images. While the conventional image clearly shows the strongly absorbing metal parts, other details are more clearly visible in the phase-contrast image. They seem to be related mainly to the structure in the plastic cover of the phone.

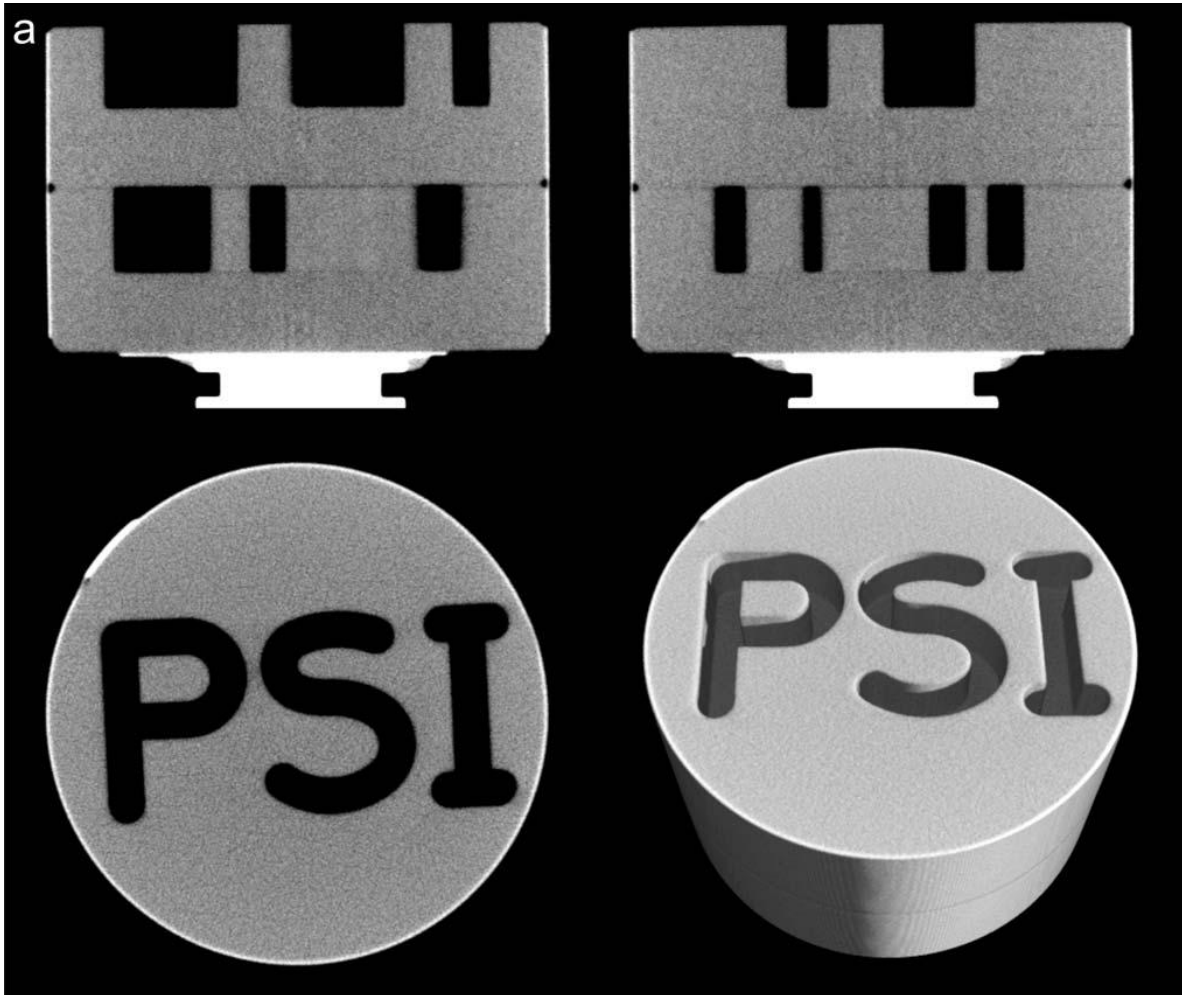


Fig. 3. CT reconstructions of a PMMA phantom. Shown are the (a) conventional reconstruction and (b) the phase-contrast reconstruction. The phantom consists of a PMMA cylinder of 30 mm diameter. The text "PSI" was milled into the cylinder on a CNC machine. Contrast is obtained between the air-filled letters and PMMA. Shown are cross sections for three orthogonal directions, the reconstructed slice (bottom left) and two longitudinal cross sections (top left, top right), as well as a 3D rendering (bottom right).

### 3.2 Tomography of a PMMA phantom

We also performed a tomography scan on a simple test phantom. The phantom was a PMMA cylinder with a diameter of 30 mm and with the text "PSI" (abbreviation for "Paul Scherrer Institut") milled into it on a CNC machine. We recorded 361 projections of  $511 \times 362$  pixels and applied the appropriate filtered-backprojection algorithms for the reconstruction of the conventional and the phase data (compare Section 1.3). The reconstructed volume measures  $511 \times 511 \times 362$  voxels. Cross sections and a volume rendering are shown in Figures 3a and 3b for the reconstruction of the conventional and the phase data, respectively.

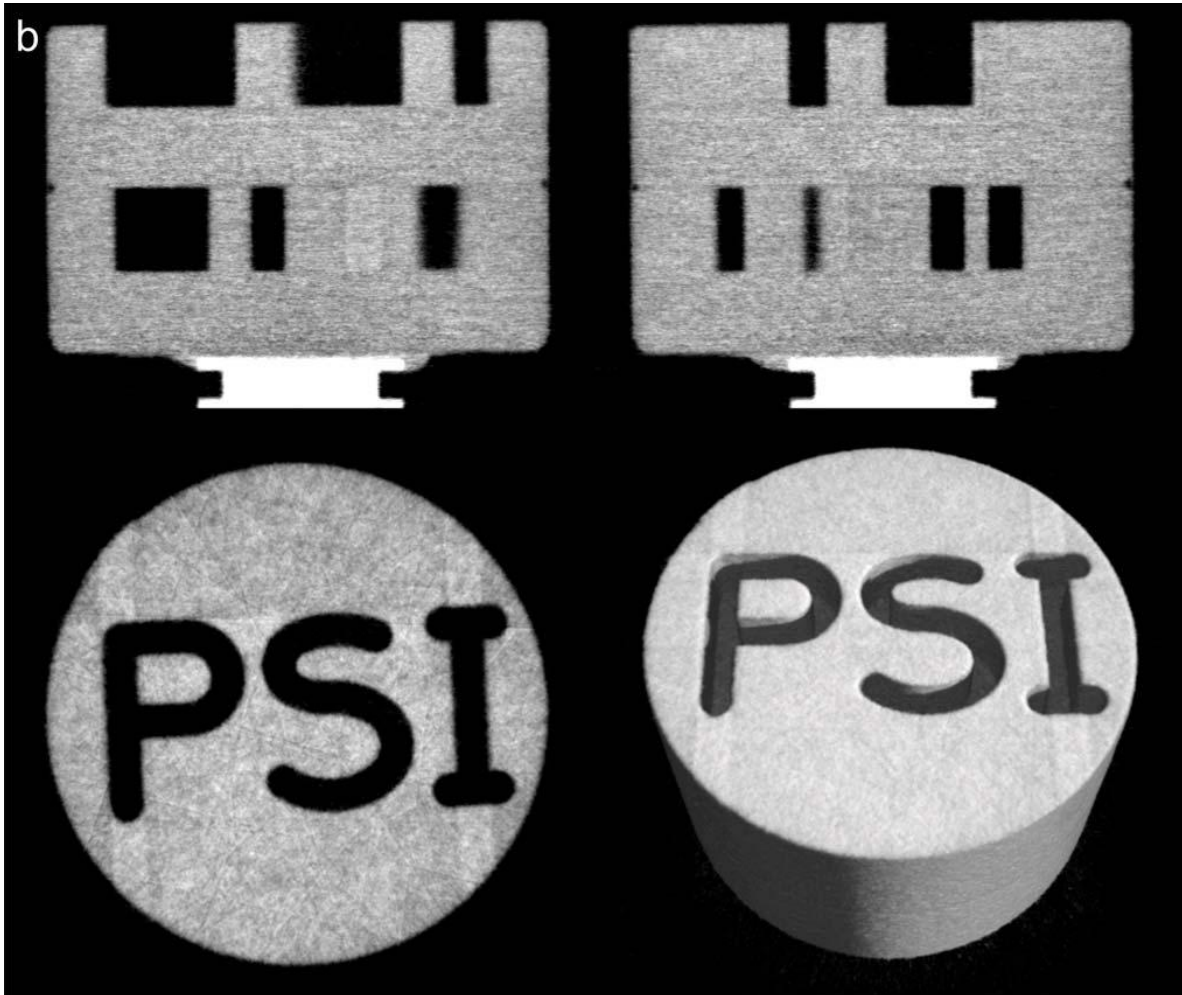


Fig. 3. (continued)

In order to verify correct operation of the grating interferometer at the design energy, we determined the effective x-ray energy at which the phase-measurement was performed. The effective x-ray energy of the measurement is the x-ray energy for which the theoretical value of the refractive index decrement  $\delta$  is equal to the measured value. Therefore, we compared the measured refractive index decrement of PMMA obtained from the phase-reconstruction with the theoretically expected  $\delta_{th}(E)$  as a function of x-ray energy. We determined mean value and standard deviation of the reconstructed  $\delta$  from one pixel over  $N = 21$  independent reconstructed slices. The obtained refractive index decrement of  $\delta = (7.1 \pm 0.2) \times 10^{-8}$  for PMMA corresponds to the theoretical value at  $E = (56.9 \pm 0.8)$  keV x-ray energy. Thus, our phase measurement was conducted with the effective x-ray energy of 56.9 keV that deviates by only  $\sim 5\%$  from the design value. This measured effective energy is a result of the x-ray spectrum, the spectral efficiency of the x-ray camera, and the spectral efficiency of the grating interferometer.

#### 4. DISCUSSION & SUMMARY

We have constructed the first x-ray grating interferometer for 60 keV x-ray energy. Thereby, we have more than doubled the x-ray energy range that is accessible for x-ray grating interferometry and interferometric phase-contrast imaging.

We could confirm that our tomographic measurements indeed result in a measurement of the refractive index decrement that corresponds to the literature values for the effective x-ray energy of 56.9 keV. The extension of phase-contrast imaging from the so far achieved 28 keV to the here achieved 60 keV allows for the investigation of significantly larger samples. As example, the 10 % transmission thicknesses for water, aluminum, and iron are given in Table 2. Increasing the x-ray energy from 28 to 60 keV, the transmission thickness of water is almost doubled to 112.6 mm. The relative increase for aluminum and iron is even bigger because of the higher Z-number of these elements. A transmission thickness of more than 100 mm in water or water-like body tissues makes phase-contrast CT in clinical applications possible. Thus, the extension to this higher energy opens up many new applications of the phase-contrast technique in medicine, but also in industry and research.

Table 2. Material thickness with 10% transmission remaining for selected materials at 28 and 60 keV. The relative increase of the transmission thickness going from 28 to 60 keV is given.

Material	10% Transmission Thickness $t_{10}$		
	$t_{10}(28 \text{ keV})$ [mm]	$t_{10}(60 \text{ keV})$ [mm]	$t_{10}(60 \text{ keV}) / t_{10}(28 \text{ keV})$
Water (H <sub>2</sub> O)	57.3	112.6	1.97
Aluminum (Al)	6.5	31.0	4.80
Iron (Fe)	0.30	2.5	8.36

## REFERENCES

- [1] Weitkamp, T. et al., "Quantitative X-ray phase imaging with a grating interferometer," *Opt. Express* 13, 6296-6304 (2005).
- [2] Momose, A. et al., "Phase Tomography by X-ray Talbot Interferometry for Biological Imaging," *Japanese J. Appl. Phys.* 45(6A), 5254-5262 (2006).
- [3] Pfeiffer, F., Weitkamp, T., Bunk, O., and David, C., "Phase retrieval and differential phase-contrast imaging with low-brilliance X-ray sources," *Nature Phys.* 2, 258-261 (2006).
- [4] T. Weitkamp, C. David, C. Kottler, O. Bunk, and F. Pfeiffer, "Tomography with grating interferometers at low-brilliance sources," *Proc. SPIE* 6318, 63180S1-10 (2006).
- [5] Pfeiffer, F. et al., "High-resolution brain tumor visualization using three-dimensional x-ray phase contrast tomography," *Phys. Med. Biol.* 52, 6923-6930 (2007).
- [6] Pfeiffer, F. et al., "Hard X-Ray Phase Tomography with Low-Brilliance Sources," *Phys. Rev. Lett.* 98, 108105 (2007).
- [7] Pfeiffer, F. et al., "Hard-X-ray dark-field imaging using a grating interferometer," *Nature Materials* 7, 134-137 (2008).
- [8] Faris, G.W. and Byer, R.L., "Three-dimensional beam-deflection optical tomography of a supersonic jet," *Appl. Opt.* 27, 5202-5212 (1988).
- [9] David, C. et al., "Fabrication of diffraction gratings for hard X-ray phase contrast imaging," *Microelectron. Eng.* 84, 1172-1177 (2007).